

Rapid and Flexible Humidity Sensor Based on Laser-Induced Graphene for Monitoring Human Respiration

Changung Paeng, Arunkumar Shanmugasundaram, Gunwoo We, Taewook Kim, Jongsung Park, Dong-Weon Lee,* and Changyong Yim*



Cite This: *ACS Appl. Nano Mater.* 2024, 7, 4772–4783



Read Online

ACCESS |



Metrics & More



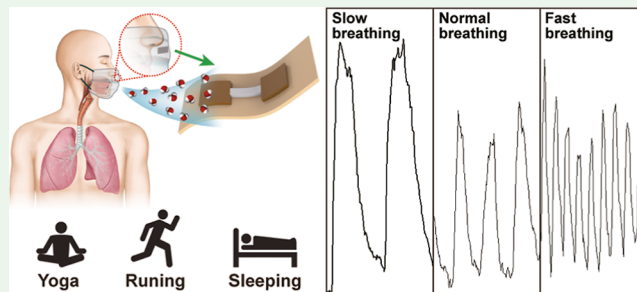
Article Recommendations



Supporting Information

ABSTRACT: Respiration is an important physiological parameter used to assess human health and metabolic activity. Herein, we propose a laser-induced graphene (LIG)-based humidity sensor for respiratory monitoring. This sensor is fabricated through a combination of laser irradiation and intense pulsed light (IPL) sintering techniques. Initially, an ink containing copper nanoparticles (CuNPs) and graphene nanoplatelets (GnPs) is coated onto a polyimide (PI) substrate. The LIG is formed on the PI film using laser irradiation. To establish a reliable electrical connection between the LIG and the copper electrode, the ink undergoes rapid IPL sintering, resulting in an IPL-sintered copper electrode. This technique not only optimizes the fabrication process but also obviates the need for traditional approaches, such as copper wire bonding, electrode patterning, or the application of conductive paint on the LIG sensor. The humidity-sensing capabilities of the sensor are assessed under various relative humidity (RH) conditions. The sensor's response escalates from roughly 15 to 92% as RH levels increase from 13 to 67%. The sensor showed minimal response to various potential interfering gases like ammonia, ethanol, carbon monoxide, sulfur dioxide, and nitrogen dioxide (with responses of 0.4, 1.87, 0.102, 0.12, and 0.29%, respectively), confirming its high selectivity for RH (91.2%). Additionally, the sensor demonstrates exemplary reproducibility, as evidenced by its consistent responses (approximately 47.65, 49.13, 48.65, 49.09, and 49.39) over five cycles at 40% RH. The LIG sensor is used to monitor a wide range of respiratory patterns, including normal, slow, fast, and apnea events. The sensor effectiveness is proven through the consistent detection of human breathing patterns over 30 min, demonstrating its stability and reliability for extended use in continuous respiratory monitoring. These findings highlight the significant potential of LIG sensors as advanced precision devices in clinical respiratory monitoring with potential integration into modern medical practices.

KEYWORDS: laser-induced graphene, intense pulsed light sintering, humidity sensing, respiration monitoring, biomedical device



INTRODUCTION

Respiration monitoring is essential in the field of human health monitoring and activity tracking.^{1–3} Spirometry and airflow meters have been widely used in the healthcare sector to diagnose various respiratory diseases such as chronic obstructive pulmonary disease, asthma, pneumonia, and sleep apnea.⁴ However, the effectiveness of these techniques strongly depends on the patient's understanding, cooperation, and effort. Performing the maneuvers correctly can be challenging, especially for children, elderly individuals, or those with cognitive impairments.^{5–7} Furthermore, these traditional medical devices have yet to achieve real-time and portable monitoring capabilities.⁶ Thus, while these methods are useful, their limitations demand the need for ongoing improvements in this field.

Over the years, several methods for monitoring respiration have been proposed. One approach that has garnered significant attention in the scientific community involves monitoring the humidity in exhaled human breath.⁸ To

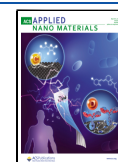
enhance the performance of humidity sensors, researchers have explored various sensing materials, including metal oxide semiconductors,^{9,10} conjugated polymer materials,^{11,12} paper-based materials,^{13,14} ionic polymers,¹⁵ and two-dimensional (2D) materials. However, only a few of these materials meet the criteria for sensitive, selective, and wearable technology. For instance, metal oxide-based sensors often require a heater and temperature control during the dehydration process.¹⁵ Conjugated polymer materials present several challenges, such as long-term instability, prolonged response/recovery times, limited moisture absorption, and air permeability.¹⁶ While paper-based sensors represent a relatively novel approach, they

Received: November 5, 2023

Revised: January 30, 2024

Accepted: February 1, 2024

Published: February 16, 2024



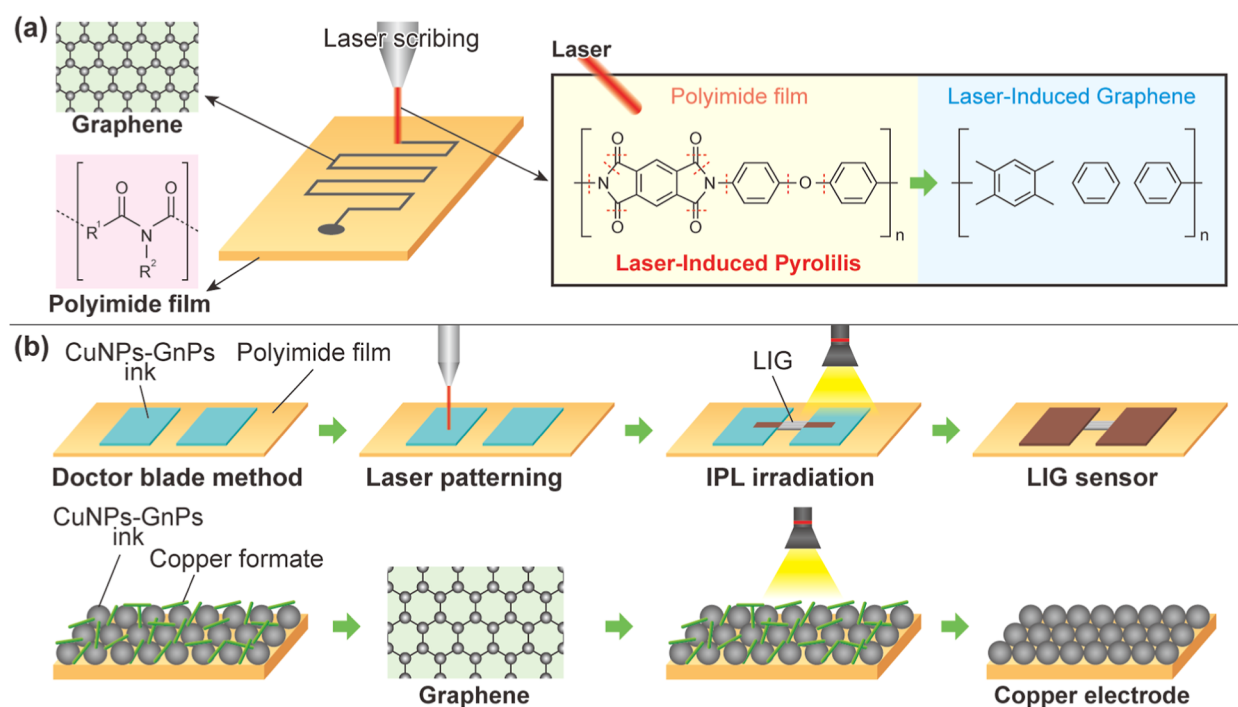


Figure 1. Schematic illustrating the fabrication process of a LIG sensor. (a) Mechanism involved in the formation of LIG on the PI substrate. (b) Schematic demonstrating the realization of the LIG sensor using laser patterning followed by an IPL-sintered copper electrical pad on the PI substrate.

are hindered by their fragility and propensity to wrinkle when wet.¹⁴ Ionic polymer materials might deteriorate or degrade over time under specific environmental conditions, potentially affecting sensor performance.¹⁷ While 2D materials, such as WS_2 ,¹⁸ MoS_2 ,⁹ and MoO_3 ,¹⁹ are prevalent in humidity sensors, the integration of these materials into flexible substrates suitable for wearable technology poses significant challenges, limiting their practical applicability and long-term stability.

Recently, graphene-based humidity sensors have garnered substantial interest owing to their exceptional chemical and physical properties.²⁰ Among various graphene forms, laser-induced graphene (LIG) has received considerable attention owing to its high electrical conductivity (5–25 S/cm) and large specific surface area ($\sim 340 \text{ m}^2/\text{g}$).^{20–22} To date, several research efforts have been made to produce LIG from diverse materials such as thermoplastic polymers, biopolymers, paper, cellulose, wood, and cork.^{23–25} Its versatility and potential have been demonstrated in several applications, including disposable pH electrochemical sensors²⁴ and electronic applications.²⁵ Of special interest has been the recent rise in the fabrication of LIG sensors for airflow sensing.^{26–28} This interest is due to their 3D porous structure inherent to LIG, which enhances the penetration and diffusion of water vapor, enabling interaction with a larger portion of the graphene surface and thereby enhancing the performance of the sensor.^{21,29} For instance, Stanford et al. proposed flexible and embeddable LIG sensors on a polyimide (PI) substrate to rapidly fabricate flexible arrays of gas sensors that detect a broad range of gases based on their thermal conductivity.²⁶ Huang et al. proposed a novel application of an LIG hydroelectric generator, powered by human breath for breath analysis and bacterial killing.²⁷ When the LIG sensor is exposed to human breath, it generates an electrical potential that changes with varying humidity levels, providing a self-reporting feature for mask condition monitoring. In another

study, the authors proposed the LIG sensor with poststructural biomimicry as an ultrasensitive, fast-responsive, directional airflow sensor.²⁸ Zhu et al. proposed a sandwich-structured humidity sensor employing LIG as an interdigital electrode.³⁰ Subsequently, a graphene oxide (GO) solution was drop-coated onto the LIG electrodes, establishing the sensitive layer. In a similar vein, Lan et al. fabricated a humidity sensor by drop-casting a GO aqueous solution onto the surface of a LIG interdigitated electrode.³¹

Nonetheless, the existing LIG-based sensors predominantly rely on the physical adsorption of the sensitive layer onto the electrodes, compromising the electrical performance reliability. Establishing robust electrical connections with electrode pads or wires is critical for fabricating the LIG. Conventional methodologies for achieving these connections, such as the utilization of silver paint or conductive epoxy, are intricate and labor-intensive.^{26,32–34} Moreover, the traditional manual connection process employing these conductive materials often results in an inconsistent output. Such limitations hinder LIG from fully realizing its potential in sensor device fabrication and demand the necessity for alternative technological approaches capable of streamlining the process and reducing costs.

In this study, we introduce a novel fabrication method that employs laser irradiation and intense pulsed light (IPL) sintering to fabricate a LIG sensor on a PI substrate. This chemiresistive-based LIG sensor is designed to detect RH and various human respiration patterns. The method involves using a $10.6 \mu\text{m}$ CO_2 laser beam with a power density of 3 W and IPL sintering at 4333 W to construct both conductive copper films and LIG on the thermally sensitive PI substrate. In stark contrast with traditional thermal sintering methods requiring high thermal conductivities, IPL sintering employs brief, high-intensity broad-spectrum light pulses to swiftly elevate the copper nanoparticles (CuNPs) to their sintering temperature.

This rapid procedure, completed within seconds, presents a compelling proposition for the large-scale manufacturing of printed electronics. Additionally, incorporating IPL sintering mitigates the environmental footprint of device fabrication by circumventing the generation of toxic chemical waste typically associated with orthodox photolithographic processes. The structural and compositional characteristics of the LIG on the PI substrate were meticulously analyzed using techniques such as electron microscopy (in both scanning and transmission modes), X-ray diffraction (XRD), FTIR, Raman spectroscopy, and XPS. These analyses confirmed the consistency and reliability of our fabrication approach. We sincerely believe that the proposed LIG sensor holds significant potential as a diagnostic tool in biomedical applications, particularly in the surveillance of diseases associated with respiratory functions.

■ EXPERIMENTAL SECTION

Materials. PI film (IM301451, thickness: 125 μm , grade: DuPont Kapton FPC) was purchased from GoodFellow Co. Ltd.; CuNPs, graphene nanoplatelets (GnPs), polyvinylpyrrolidone (($\text{C}_6\text{H}_9\text{NO}$) $_n$), formic acid (HCOOH), and diethylene glycol ((HOCH_2CH_2) $_2\text{O}$) were purchased from Sigma-Aldrich Co. Ltd.

Mechanism Involved in the Formation of LIG on the PI Substrate. PI is a widely utilized material for the fabrication of LIG owing to its exceptional thermal stability and mechanical properties. The chemical structure of PI comprises two essential components: the imide group and the aromatic moiety. The imide group consists of two carbonyl ($\text{C}=\text{O}$) groups attached to a nitrogen (N) atom, while the aromatic moiety typically consists of a benzene ring connected to the imide group. Upon exposure of the PI substrate to a laser with a specific wavelength, the PI material absorbs the incident laser energy. This absorption process leads to a series of photochemical effects and localized heating within the substrate. The underlying mechanism primarily involves photochemical effects, as the energy carried by the photons (ranging from 300 to 1196.6 kJ/mol) is comparable to the bond energies of organic compounds. As a result, chemical bonds within the PI, such as C–C bonds (with bond energies of 320.2–493.9 kJ/mol) and C=C bonds (with bond energies of 610–735 kJ/mol), can be broken.^{35,36} The localized heating induced by the laser energy triggers thermal decomposition of the PI material, leading to the formation of laser-induced pyrolysis. During this process, the PI undergoes significant chemical transformations, resulting in the generation of carbon-rich species predominantly composed of carbon atoms. These carbon atoms subsequently undergo recombination and rearrangement, ultimately giving rise to the formation of a graphene-like structure on the surface of the PI film, as shown in Figure 1a.

Fabrication of LIG Sensor and Laser-Sintered Copper Pads. The formation of LIG and the fabrication of laser-sintered copper pads on the PI substrate are schematically illustrated in Figure 1b. The fabrication process began by homogeneously mixing 490 mg of CuNPs, 10 mg of GnPs, and 0.75 mL of formic acid using a vortex. Subsequently, 60 mg of polyvinylpyrrolidone and 1 mL of diethylene glycol were added to the mixture and thoroughly blended using a vortex and sonication, resulting in the formation of a homogeneous CuNPs/GnPs ink. A doctor blade technique was employed to coat the CuNPs/GnPs ink paste onto the PI substrate. Following this, the coated substrate was annealed on a hot plate at 130 $^{\circ}\text{C}$ for 20 min to facilitate solvent evaporation. Subsequently, the CuNPs/GnPs paste-coated PI substrate was positioned on a commercial Universal Laser Systems instrument for the formation of LIG. The substrate was placed 2 cm away from the laser source with a power density of 3.0 W. A laser with a scanning rate of 6 mm/s was employed to simultaneously induce the formation of graphene on the PI substrate and sinter a portion of the CuNPs/GnPs pad. Upon completion of the LIG formation, the substrate was subjected to IPL exposure to generate conductive copper pads with strong electrical connections to LIG. The IPL exposure (4333 W) was carried out at room

temperature (25 $^{\circ}\text{C}$) in an ambient atmosphere with an exposure time of 6 ms.

Details of Experiments and Characterization Techniques.

The morphological characteristics of the LIG and copper pads were analyzed using field emission scanning electron microscopy (FESEM) (model JEOL JSM-7500F) at a working distance of 15 mm and with an electron beam energy of 10 keV. Additionally, transmission electron microscopy (TEM) (JEM-2100F HR-TEM) was employed for detailed structural examination. For TEM analysis, the samples were first dispersed in ethanol through ultrasonication, following which they were placed on a carbon support film adhered to a 150-mesh nickel grid. The samples were then examined at an acceleration voltage of 200 kV. The crystalline structure of the sample was ascertained using powder XRD analysis. This analysis was conducted on an X-Pert Pro diffractometer, which employs a Cu $K\alpha$ radiation source with a wavelength of 0.15406 nm. The instrument settings were maintained at 40 kV and 30 mA, and the analysis incorporated a standard monochromator equipped with a Ni filter to ensure a precise measurement. Confocal micro-Raman spectra were acquired by employing a Horiba Jobin-Yvon LabRam HR spectrometer equipped with a 17 mW internal He–Ne laser (632.8 nm excitation). Fourier transform infrared spectroscopy was conducted by using a Spectrum 400 spectrometer. X-ray photoelectron spectroscopy (XPS) analyses were conducted by using the ESCALAB 2 spectrometer (VG Scientific, UK). The analysis chamber's base pressure was meticulously maintained at 5×10^{-10} mbar, with a slight increase to 2×10^{-8} mbar during the actual measurements. These experiments utilized an Al $K\alpha$ X-ray source, which is nonmonochromated, with the excitation energies set at 1486.6 eV. The acquired data were processed by using the SpecsLab2 CasaXPS software (Casa Software Ltd.). For energy-scale calibration, we normalized the C 1s peak of the hydrocarbons to 285.0 eV to ensure accuracy in our measurements.

Gas sensing analysis was conducted by using humidified air as the target gas. Humidified air was produced by managing the flow rates of two separate gas streams: dry air and air saturated with moisture from the bubbler. Experiments were conducted under controlled conditions with a constant gas flow rate of 200 sccm. Different flow rate ratios yielded various RH levels, while the combined flow rate for both channels remained constant at 200 sccm. For instance, 0% RH was achieved with a 200 sccm flow of dry air and no flow of wet air, whereas 13% RH was realized with a 175 sccm flow of dry air combined with a 25 sccm flow of wet air. The sensors were tested in a controlled environment with a stable temperature of 25 $^{\circ}\text{C}$ and varying humidity levels ranging from 13 to 67% RH under normal atmospheric conditions. These conditions were maintained consistently across all experiments to ensure reliable data. Interfering gases such as NO_2 , SO_2 , NH_3 , CO, and EtOH were introduced at a rate of 10 sccm and then diluted using a 190 sccm air flow. The gas sensing setup comprised a data acquisition system (GMC-1200, ATOVAC, Korea) and a temperature control unit (MST-1000H, MSTECH, Korea). The RH of the resulting humid air was determined by using a commercial humidity sensor (DHT-11). The sensor's resistance was continuously monitored in real time as a function of time using a Keysight BenchVue system equipped with a digital multimeter (Keysight 34461A).

■ RESULTS AND DISCUSSION

Copper electrodes are widely used in various electrical and electronic applications due to their superior electrical conductivity. However, they are susceptible to thermal oxidation; therefore, an ink based on a CuNPs/GnPs hybrid composite was prepared to fabricate large area copper electrode pads. The excellent thermal conductivity of GnPs can help to dissipate heat more effectively and prevent the onset of thermal oxidation. First, the impact of the CuNPs and GnPs composition on the resistance of the conductive pad is examined by varying the weight percentage composition of GnPs and CuNPs (Figure S1, Table S1). The weight

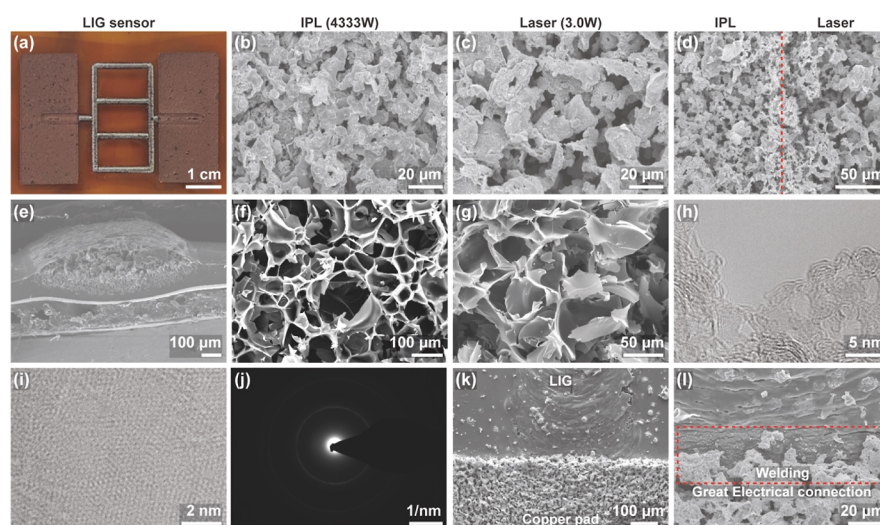


Figure 2. Morphological analysis of the LIG sensor. (a) Photograph of the fabricated LIG sensor. (b,c) FESEM images of IPL and laser-sintered CuNPs, respectively. (d) FESEM micrograph depicting the interface between IPL-sintered CuNPs and laser-sintered CuNPs. FESEM micrographs of the LIG: (e) at lower magnification and (f,g) at higher magnification. (h,i) HR-TEM images of the LIG. (j) SAED pattern was obtained from the LIG. FESEM micrographs illustrating the interface between LIG and copper electrode: (k) at lower magnification and (l) at higher magnification.

percentages of CuNPs to GnPs in the hybrid inks were set as follows: 100:0, 98:2, 96:4, 94:6, and 92:8, respectively. Among these compositions, the CuNPs/GnPs hybrid ink with a composition of 98:2 demonstrated higher thermal oxidation resistance compared to that of the other hybrid compositions.

We fine-tuned the laser power density while maintaining a constant scan speed of 6 mm/s to optimize the sensor resistance. At lower laser power settings, we observed successful copper sintering without complications, but the generation of LIG was incomplete, as shown in Figure S2a. In contrast, higher laser power settings led to the risk of burning out both the copper electrode and LIG. Moreover, we noted that the sensor resistance stabilized within a range of 300–400 Ω when operating at a laser power of 3 W. Sensors fabricated with laser powers deviating from 3 W (either lower or higher) demonstrated suboptimal resistance values, as shown in Figure S2b. Consequently, we established that a laser power setting of 3.0 W, in conjunction with a scan speed of 6 mm/s, is optimal for the defect-free and efficient production of both LIG and laser-sintered copper.

Figure 2a shows a photograph of the fabricated sensor, showcasing the formation of an LIG and its integration with the large area copper pads. Importantly, both the copper pads and the LIG exhibit a defect-free structure, indicating successful fabrication processes. Prior to the exposure to IPL, the films exhibited rod-shaped structures, along with the presence of CuNPs and GnPs (Figure S3). The formation of these rod-shaped structures results from a reaction occurring between formic acid and CuNPs. Upon exposure to the IPL, these rod-shaped structures vanish, and the nanoparticles undergo sintering due to the thermal effects induced by the IPL.^{37,38} The XRD profiles of various CuNPs/GnPs composites with differing compositions (100:0, 98:2, 96:4, 94:6, and 92:8) before and after IPL sintering are shown in Figure S4. The XRD pattern of the CuNPs/GnPs composite with a 100:0 composition exhibits distinct peaks at 43.2, 50.4, and 74.1°, aligning with the (111), (200), and (220) planes of the crystalline CuNPs, respectively. With an increase in the GNP concentration within the composite, new diffraction peaks arise at 22.4 and 45.1°, matching the (002) and (100) crystal

planes of a graphitic structure, respectively. Figure 2b, c shows the FESEM images of the IPL and laser-sintered CuNPs. Specifically, the CuNPs near the LIG experience sintering before the other areas are subjected to IPL sintering. The interface between the copper pads, which are formed through IPL, and the laser source is presented in Figure 2d. A comparison reveals that the CuNPs sintered via a laser exhibit larger particle sizes compared to those sintered using the IPL method.

The high-resolution FE-SEM images provide a cross-sectional view of the LIG, confirming the successful formation of three-dimensional (3D) porous structures on the PI substrate (Figure 2e). The PI film utilized in our experiments has a baseline thickness of 125 μm . Upon exposure to a 3.0 W, 6 mm/s, CO₂ laser during the LIG fabrication process, the overall thickness of the substrate increases to approximately 280 μm . During the laser irradiation, the energy intensity is most pronounced at the surface of the substrate, decreasing progressively with depth. This gradient results in lower temperatures beneath the surface, leaving the deeper PI film layers largely unaltered. The remaining unconverted PI film exhibits a thickness of about 50 μm . Above this layer, there exists a transition zone of approximately 70 μm thickness, characterized by partial transformation into LIG. The uppermost layer, consisting of purely converted LIG, is about 160 μm thick. This stratification of layers suggests a penetration depth of the laser's effect to be around 75 μm into the PI substrate. It is observed that the unreacted PI layer beneath the LIG serves as a structural support, providing stability to the LIG layer. Figure 2f,g, depicts crumpled graphene nanosheets with a hierarchical 3D structure. These crumpled graphene nanosheets contribute to the unique morphology of the LIG, providing an enhanced surface area and structural integrity. TEM images enable direct visualization of the LIG structure, which consists of a disordered arrangement of randomly oriented few-layer graphene sheets. Moreover, the high-resolution TEM image reveals lattice fringes with a spacing of 0.34 nm, corresponding to the (002) plane of the carbon lattice (Figure 2h).^{39,40} Scanning transmission electron microscopy images provided detailed insights into the atomic

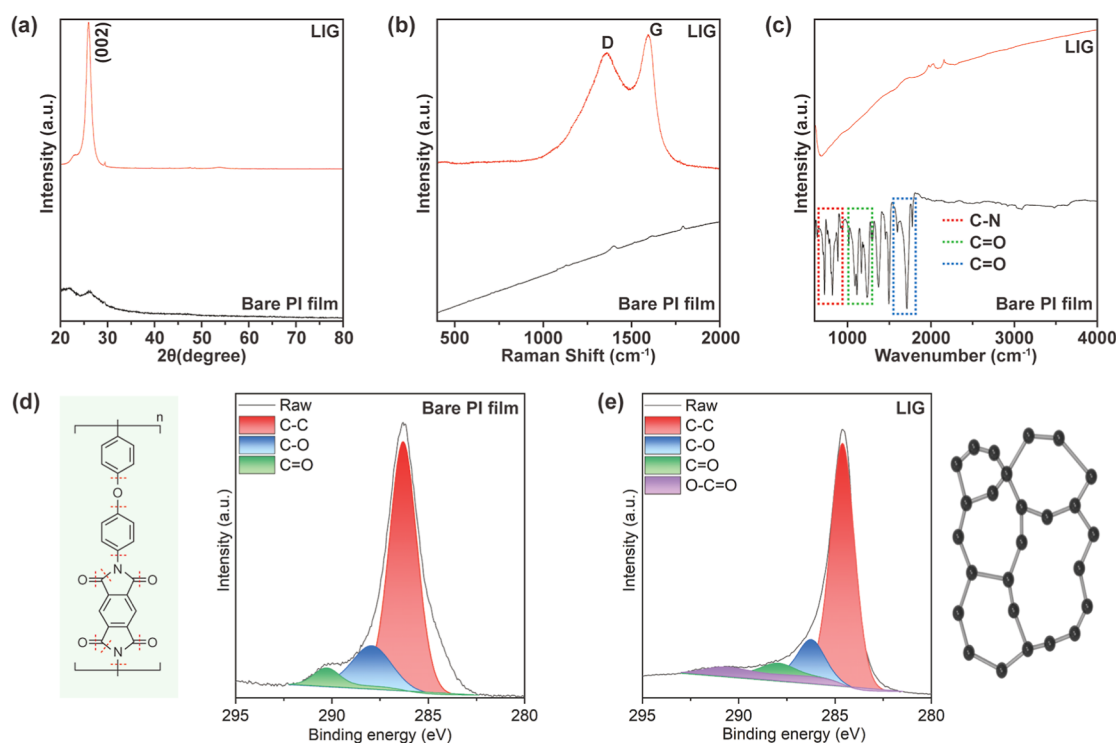


Figure 3. Crystal structure and phase purity analyses. (a) Powder XRD pattern, (b) micro-Raman spectra, and (c) Fourier transmission infrared spectra analysis of the bare PI film and the LIG. (d,e) High-resolution X-ray photoelectron spectra analysis of the bare PI and LIG in the C 1s region. The schematic shows the chemical structures of PI and the amorphous carbon crystal structure.

arrangement of carbon atoms and the overall structural characteristics of the LIG (Figure 2i). Moreover, the selected area electron diffraction (SAED) pattern of the LIG revealed diffraction spots that can be indexed to the (002) plane of the graphitic crystal structure (Figure 2j).^{41,42} Figure 2k shows a low-magnification FE-SEM image, providing visual perceptions of the interface between the LIG and the copper pad. Remarkably, the high-magnification FE-SEM image reveals an intimate fusion of the LIG and the copper pad at the interface area (Figure 2l). Further interface analysis demonstrates that IPL exposure induces the rapid heating of the CuNPs and GNPs within the hybrid ink. This intense heating leads the CuNPs to reach their melting point, enabling their fusion and the subsequent formation of conductive paths. In this process, the GNPs play a key role in enhancing the conductivity and mechanical stability of the conductive pads. By providing a conductive network within the copper matrix, the GNPs facilitate electron transfer between the copper pad and the LIG. This fusion process establishes an improved welding effect, facilitating a robust and efficient electrical connection between the LIG and the copper pad. The reproducibility, reliability, and spatial uniformity of the LIG structures produced in our process were rigorously evaluated using FESEM. This analysis was performed on LIG lines fabricated on the same substrate but at varying spatial locations as well as on samples derived from different production batches. The FESEM images demonstrated that the morphology of LIG lines, irrespective of their positions on the same substrate, exhibited remarkable consistency (Figure S5). Furthermore, a comparative analysis of LIG structures across different batches revealed minimal variation in structural characteristics, as shown in Figure S6. This slight morphological discrepancy can likely be attributed to minor fluctuations under ambient

environmental conditions and subtle differences in material handling during the fabrication process.

The crystal structure and phase purity of the LIG formed on the PI substrate were comprehensively investigated by using a range of analytical characterization techniques, as shown in Figure 3. The diffraction pattern of the PI substrate, prior to the laser scanning, exhibited broad and less intense diffraction patterns at 22.21 and 26.41°, which are indicative of its amorphous or semicrystalline nature. However, following the laser scanning, these diffraction patterns disappeared, and a new prominent diffraction peak emerged at approximately 26.5°, corresponding to the (002) plane, signifying the successful formation of a well-ordered graphitic structure on the PI substrate.^{43,44} Micro-Raman spectra of the bare PI do not exhibit any significant Raman bands (Figure 3b). However, smaller bands are observed at 1395, 1601, and 1786 cm⁻¹, which can be attributed to the presence of aromatic carbon-carbon (C-C) bonds and imide groups (C=O and C-N) within the PI structure.⁴⁵ Following the laser scanning process, the characteristic D and G bands associated with the formation of LIG become evident in the Raman spectra. The Raman band observed at 1350 cm⁻¹ indicates the presence of structural defects, such as sp³-hybridized carbon atoms and edge defects, within the LIG. Conversely, the Raman band observed at 1580 cm⁻¹, which corresponds to the well-known G band, validates the presence of sp²-hybridized carbon atoms within the LIG, signifying its graphitic nature.

FTIR spectral analysis was conducted to evaluate and compare the spectral characteristics of the bare PI film and the LIG, as shown in Figure 3c. The vibrational bands appearing in 1785, 1775, and 1772 cm⁻¹ were identified and can be indexed to the asymmetric stretching vibrations of the C=O bonds within the PI structure.⁴⁶ Furthermore, additional vibrational

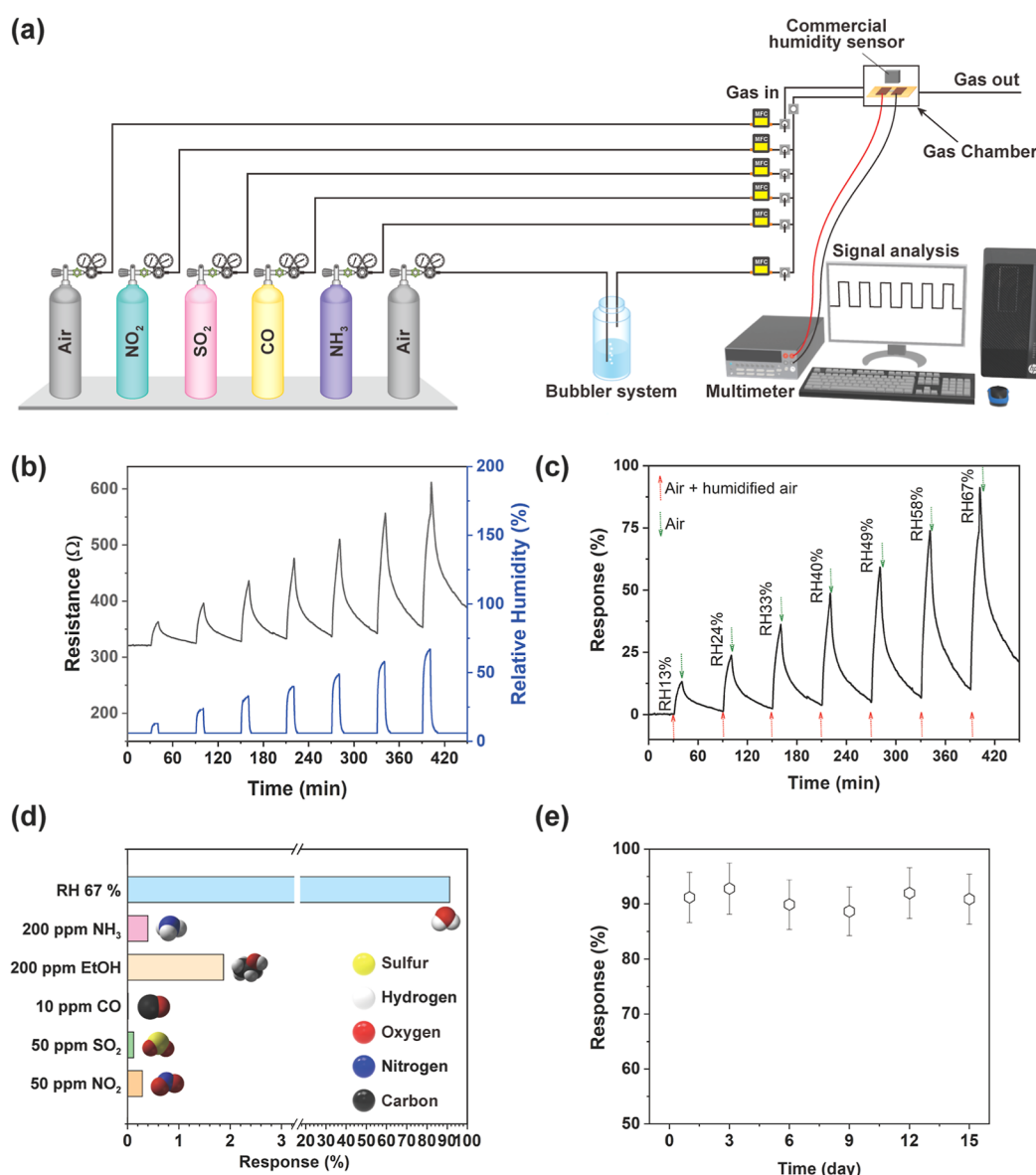


Figure 4. Humidity sensing performance of the LIG sensor. (a) Schematic representation of the experimental setup employed for gas sensing analysis. (b,c) Dynamic sensing response of the LIG sensor showcasing the variation in sensor resistance with respect to different RH levels. (d) Sensing response of the LIG sensor in the presence of other interfering gases such as NH₃, EtOH, CO, SO₂ and NO₂. (e) Long-term stability of the LIG sensor (working temperature, 25 °C, 67% RH).

bands at 1342, 1357, and 727 cm⁻¹ were observed, which can be assigned to the C–N stretching vibrations and C=O bending vibrations associated with the imide group present in PI.^{47,48} However, the characteristic functional bands of PI disappear after the laser scanning process. This phenomenon can be attributed to the localized heating and photochemical effects of laser irradiation. As a result of the absorption of the laser energy, the chemical bonds responsible for these functional bands are broken, leading to the generation of reactive intermediates. Subsequently, these intermediates undergo recombination and rearrangement processes, ultimately resulting in the formation of a graphene-like structure.

The PI substrate was thoroughly examined before and after laser scanning through XPS analysis, as shown in Figure 3d,e. The chemical structures of the PI material and the LIG are shown in Figure 3d,e. The survey spectra exhibit distinct photoelectron peaks corresponding to carbon (C 1s), nitrogen

(N 1s), and oxygen (O 1s) species (Figure S7). Notably, the photoelectron peak associated with N 1s disappears following laser scanning, indicating the rupture of the backbone imide group, which comprises two carbonyl (C=O) groups attached to a nitrogen (N) atom. The O 1s core-level spectra of both the bare PI and LIG are shown in Figure S8. In the C 1s core-level XPS spectrum of the PI and LIG, a pronounced peak corresponding to the C–C bond is observed at 284.62 eV. Additional photoelectron peaks at 286.2 and 287.9 eV are attributed to the C–O and C=O functional groups, respectively.⁴⁹ In the LIG spectrum, there is an additional peak at 290.4 eV, which can be assigned to the O–C=O functional group. Notably, in the C 1s core-level spectrum of LIG, the C–C peak is prominent compared to the bare PI. However, the intensities of the C–O and C=O peaks are significantly decreased in the LIG spectrum compared to the XPS spectrum of the bare PI substrate. This observation

strongly indicates that the LIG films predominantly consist of sp^2 carbons.³⁴ These findings are consistent with the results obtained from XRD, Raman, and FTIR spectroscopy, providing further support for the dominance of sp^2 carbon structures in the LIG films.

The flexible nature of the fabricated LIG sensor is demonstrated through resistance measurements under the conditions of bending and twisting (Figure S9). The base resistance of the fabricated LIG sensor was measured at different bending angles, such as 30 and 60°, and during manual twisting, as shown in Figure S10. The base resistance of the LIG sensor shows a minor increase as the bending angle and manual twisting intensifies, attributable to the strain applied to the LIG since graphene-based materials are known to be susceptible to applied strain. Despite the increased resistance brought on by bending and twisting, the sensor exhibits a stable base resistance, signifying the high reliability of the fabricated LIG sensor.

The experimental procedure employed for the gas sensing analysis is schematically depicted in Figure 4a. The gas-sensing measurements were conducted at 25 °C by monitoring changes in resistance under a constant applied voltage during cyclic exposure to various RH. The sensor response (S_R) of the LIG humidity sensor can be defined as⁵⁰

$$S_R = \frac{R_H - R_A}{R_A} \times 100 \quad (1)$$

where R_A and R_H represent resistance of the sensor in the presence of air and in the presence of humidity. The architecture and design of sensors are critical parameters that significantly affect their performance. To investigate this, various sensor architectures were fabricated, and their sensing properties were evaluated at an RH of 67%, as shown in Figure S11. A sensor with a single sensing line demonstrated a minimal response rate of 5%. Subsequently, a dual-line sensor was developed, which showed a marginally improved performance with a response rate of 11%, although it was still relatively low. Incorporating three horizontally aligned sensing lines resulted in a slightly higher response of 35%. However, a notable enhancement in sensing response was observed with a design consisting of four horizontally aligned sensing lines that were horizontally connected to a large copper pad, achieving a response rate of 92%. In contrast, a sensor with five sensing lines did not exhibit a significantly improved sensing response compared to the four-line sensor. The improved sensing response in designs with more lines can be attributed to the increased active area of the sensor, which enhances the efficiency of water molecule adsorption. Based on these findings, further sensing analyses were conducted using the four-line sensor design, as it exhibited the highest sensing response among the tested architectures. The sensor response was continuously monitored over time by measuring the changes in sensor resistance at different RH values, ranging from 13 to 67%. Figure 4b shows the variation of sensor resistance as a function of the RH. The sensor resistance exhibits a significant response to different levels of RH. Specifically, as the RH increases, the sensor resistance also increases. Moreover, when subjected to transitions from low to high RH levels, the sensor demonstrates excellent reversibility during exposure and recovery cycles. These characteristics indicate the sensor's capability to repeatedly and accurately sense changes in RH. Figure 4c further presents the corresponding sensing response of the LIG sensor at different

RH levels. The sensing response, quantified as the change in resistance, exhibits a substantial increase from approximately 15 to 92% when the RH levels escalate from 13 to 67%. We fabricated three distinct LIG sensors to systematically assess their sensing capabilities at varying RH levels, as depicted in Figure S12. Each sensor exhibited remarkably similar sensing responses, indicating the precision of our fabrication methodology. Specifically, the sensing responses of sensor-1, sensor-2, and sensor-3 at 67% RH were quantified as 86, 93, and 87%, respectively. Additionally, we also evaluated the reproducibility of these LIG sensors under controlled conditions of 40% RH at 25 °C, spanning five distinct cycles. The recorded sensing responses for the LIG sensors across these cycles were approximately 47.65, 49.13, 48.65, 49.09, and 49.39; 40.65, 43.22, 44.16, 45.36, and 46.27; and 44.64, 45.75, 45.90, 46.43, and 47.72; respectively, as shown in Figure S13. This analysis not only confirms the sensors' stable response and recovery characteristics but also emphasizes the robustness and consistency of our fabrication process, culminating in sensors with excellent response and recovery attributes for accurate humidity detection. Response linear fitting curves of the LIG sensors at different humidity levels at 25 °C are shown in Figure S14. The theoretical limit of detection (LOD) of the sensor was calculated using the following equation

$$LOD = 3 \times \frac{\sigma}{\text{slope}} \quad (2)$$

Herein, σ represents the standard deviation. To ascertain the σ value, a data set consisting of 30 data points from the initial phase of the response curve was analyzed. The calculated LOD for the LIG sensor was determined to be 6.1% RH, demonstrating its exceptional sensitivity in detecting low levels of RH at ambient temperature. To contextualize the sensing capabilities of the LIG sensor, we compared its performance with those of other humidity sensors reported in the literature (Figure S15 and Table 1). In this comparative analysis, our

Table 1. Humidity Sensing Performance of the LIG Sensor and That of Other Reported Humidity Sensors

material	fabrication method	RH range (%)	response (%)
LIG-CuNPs (this work)	CO ₂ laser scanning and IPL irradiation	13–67	15–92
graphene ⁵¹	CVD	12–97	1.1–4.97
PDDA/rGO ⁵²	LbL self-assembly	11–97	8.69–37.43
defect graphene ⁵³	solvothermal method	3–30	0.27–3.33
BP-graphene ⁵⁴	HEBM technique	15–70	3–43.4
Pd/HNb ₃ O ₈ ⁵⁵	cation intercalation stripping method	30–99.9	0–26
V ₂ O ₅ nanosheets ⁵⁶	hydrothermal method	11–97	45.3
NCQDs ⁵⁷	hydrothermal method	10–95	90.97
MWCNTs ⁵⁸	drop and dry	0–91.5	1.06
ZnO nanosheets ⁵⁹	chemical water bath method	11.3–97.3	86

LIG sensor demonstrated superior sensing attributes relative to other sensors such as graphene,⁵¹ PDDA/rGO,⁵² defect graphene,⁵³ BP-graphene,⁵⁴ Pd/HNb₃O₈,⁵⁵ V₂O₅ nanosheets,⁵⁶ NCQDs,⁵⁷ MWCNTs,⁵⁸ and ZnO nanosheets,⁵⁹ particularly in terms of enhanced sensing response.

The sensor's selectivity, a key parameter of its sensing response, plays a pivotal role in its functionality. Hence, the

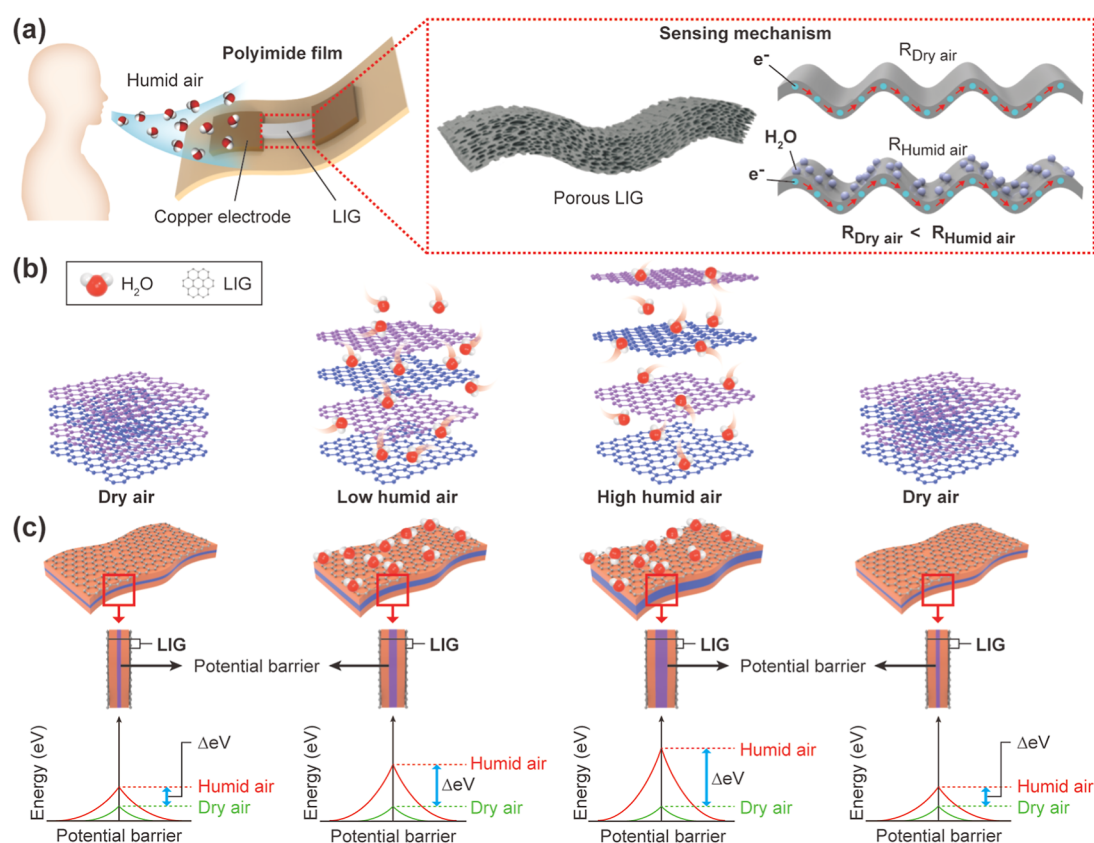


Figure 5. (a–c) Schematic representation of the physical model, accompanied by the energy band diagram, detailing the sensing mechanism of the LIG sensor under both dry and humid air conditions.

LIG sensor's selectivity was measured in the presence of various target gases, including ammonia (NH₃), ethanol (CH₃CH₂OH), carbon monoxide (CO), sulfur dioxide (SO₂), and nitrogen dioxide (NO₂), each at a concentration of 200, 200, 10, 50, and 50 ppm, respectively (Figures 4d and S16). The LIG sensor showed minimal sensing response of 0.4, 1.87, 0.102, 0.12, and 0.29% to NH₃, CH₃CH₂OH, CO, SO₂, and NO₂, thus demonstrating its high selectivity for RH (91.2%) over these potential interfering gases. A sensor's longevity and consistent performance, denoted as long-term stability, are crucial factors for its practical application. Consequently, we assessed the sensor's response to a 67% RH level, taking measurements at specified time intervals over a duration of 15 days. The recorded sensor responses were consistently within the range of 91.25 ± 4.61 throughout this period, thereby signifying the sensor's long-term stability (Figure 4e).

The increase in resistance of the LIG sensor upon exposure to humidity can be explained based on the physical model and energy band diagram depicted in Figure 5. First, the LIG has a unique porous structure with a high surface area, which is beneficial for sensing applications. The structure of the LIG provides numerous active sites for the adsorption of water molecules. This high surface area allows more water molecules to interact with the sensor, enhancing its sensitivity to humidity. Water molecules have a strong dipole moment and can form hydrogen bonds. When humidity comes into contact with the LIG, water molecules are adsorbed onto the surface through physical adsorption (van der Waals forces) and chemical adsorption (hydrogen bonding). Such adsorbed water molecules can perturb the conductive properties of

LIG.⁶⁰ Specifically, water molecules might either introduce doped charges or adsorb onto the graphene surface, leading to alterations in electron distribution and consequently, modifications in conductivity (Figure 5a). Moreover, the rise in LIG resistance is influenced by a swelling effect.⁶¹ As water molecules adsorb onto LIG, they cause the interlayers to swell, which subsequently increases the spacing between the graphene sheets (Figure 5b). This increased interlayer distance in a humid environment raises the potential barrier when compared with the potential barrier in dry air. An increase in humidified air concentration further intensifies this potential barrier between the graphene layers, reducing connectivity and resulting in an increase in resistance. When the sensor is exposed to dry air, the inherent high porosity of LIG allows dry air to flow through its structure, thereby desorbing the attached water molecules and reverting it to its original configuration (Figure 5c). The high sensitivity and selectivity of LIG sensors toward humidity as compared to other interfering gases like NH₃, EtOH, CO, SO₂, and NO₂ can be attributed to several factors inherent in the properties of LIG and the nature of humidity interactions. As discussed earlier, the porous structure of LIG adsorbs significantly more humidity compared to other interfering gases, leading to a more pronounced sensor response. The excellent selectivity of LIG toward humidity can be attributed to the affinity of graphene-based materials for polar molecules like water, as opposed to less polar or nonpolar gases like NH₃, EtOH, CO, SO₂, and NO₂. Therefore, the water molecules can lead to a significant change in the electrical properties of LIG due to the water's polar nature, which is more pronounced than the effect of other nonpolar or less polar gases. In addition, in a typical experimental

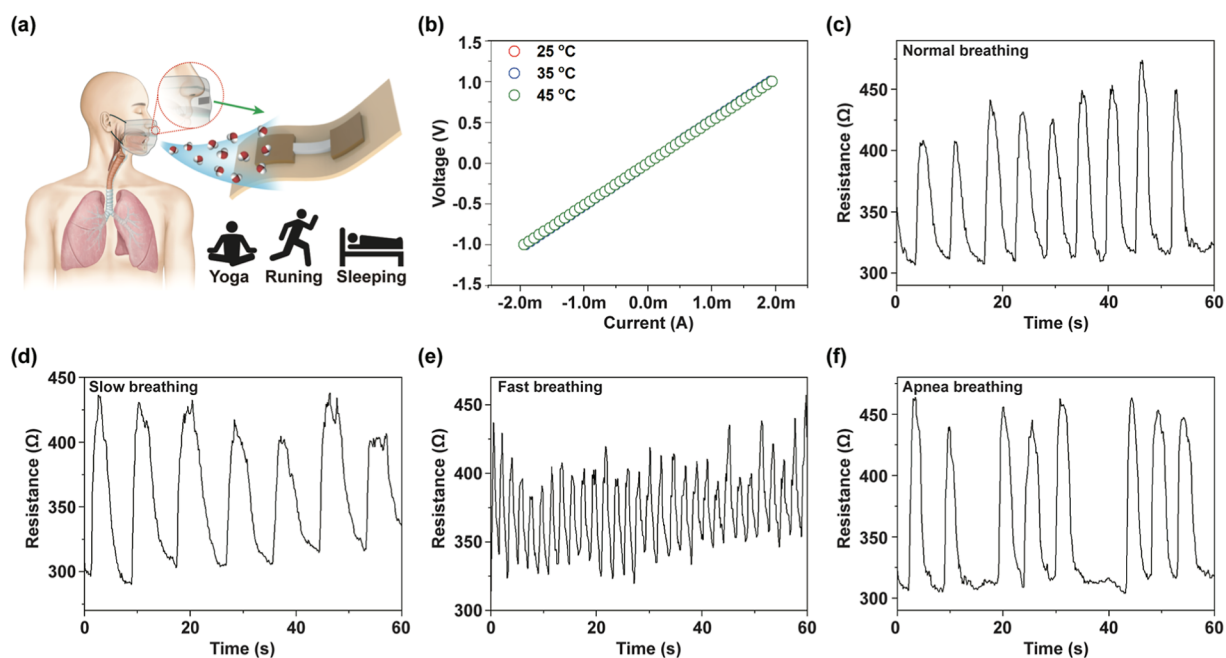


Figure 6. (a) Schematic of breath sensing analysis. (b) Current versus voltage characteristics of the LIG sensor at three different temperatures. (c–f) Investigation of the LIG sensor's response behavior under varying respiratory patterns, including slow, normal, fast, and alternating periods of respiration and apnea.

condition, the concentration and variation of humidity were higher compared to those of these other gases. This makes the sensor more responsive to changes in the humidity levels. The surface of LIG can be chemically modified or functionalized to enhance its sensitivity to specific molecules like water. Such modifications might make the sensor less responsive to other gases due to reduced interaction or adsorption sites for these molecules.

Finally, the fabricated LIG sensor was used to monitor respiration. Figure 6a shows a photograph of a volunteer outfitted with a medical respirator mask in which a LIG-based wearable humidity sensor is securely integrated. The sensor operates at a low driving voltage, typically in the range of 1.5 V. This value was chosen based on a balance between achieving optimal sensitivity for humidity detection and ensuring that the voltage remains within safe limits for human use. To facilitate the detection of human respiration, the humidity sensor was securely affixed beneath the human nose using a commercially available scotch tape or positioned within a medical mask. The temperature difference in human breath during inhalation and exhalation ranges between 10 and 15 °C. Therefore, we evaluated the influence of temperature variation on the electrical performance of the LIG sensor. This was achieved by measuring the current–voltage (I – V) characteristics of the LIG sensor under different temperatures such as 25, 35, and 45 °C (Figure 6b). The I – V curves demonstrated consistent behavior across three disparate temperature conditions, thereby indicating that variations in breathing temperature do not significantly affect the sensor's response. Additionally, based on the selectivity analysis results, we can infer that the impact of other interfering gases present in human breath on the humidity sensor can be neglected. Figure 6c shows the real-time traces illustrating the dynamic changes in resistance of the LIG humidity sensor in response to human breath.

The sensor's resistance was continuously monitored during multiple inhaling and exhaling breath cycles. The fabricated

LIG sensor demonstrated a remarkable capability to monitor respiration patterns over an extended period (Figure S17). The sensor successfully detected human breathing patterns consistently for a duration of 30 min. This prolonged detection ability highlights the sensor's stability and reliability, making it suitable for applications in continuous respiratory monitoring. The sensor's consistent performance over this time frame suggests its potential utility in healthcare applications, where long-term respiratory monitoring is crucial. Notably, an increase in resistance was observed during exhalation, followed by recovery to its initial resistance level before the subsequent exhalation. This behavior highlights the sensor's ability to detect and respond to the moisture content present in exhaled breath. Figure 6d,e depicts the sensing response of the LIG sensor under various respiratory patterns encompassing slow and accelerated breathing rates. The sensor signals exhibit a smooth profile with slow and normal respiratory rates (minor fluctuations appearing to be nearly negligible). In contrast, rapid respiration results in sensor signals that are narrow and distinctly sharp due to the accelerated frequency. The three distinct respiratory rates (slow, normal, and fast) can be easily discriminated by assessing the interval between two adjacent peaks in the sensing signal. The observed respiratory periodicities of the volunteer at slow, normal, and rapid paces were found to be 10, 5, and 1.4 s, respectively. Figure 6f shows the LIG sensor's response characteristics during successive respiration and apnea periods. The constancy of the relative resistance observed during the apnea phase signifies that the sensor is predominantly responsive to fluctuations in humidity levels. This feature could potentially be employed in the detection of symptoms related to sleep apnea. The durations of inhalation, exhalation, apnea, and different respiration rates can be ascertained from variations in sensor resistance during the respective respiration conditions. This signifies that the proposed LIG sensor could be utilized as

a medical diagnostic device to monitor respiratory-related diseases.

CONCLUSIONS

We proposed a high-performance humidity sensor based on LIG for respiratory monitoring. The fabrication process involved laser irradiation, followed by IPL sintering. The laser irradiation phase results in the formation of a porous 3D graphene network on the PI substrate. This is followed by IPL sintering, which ensures a robust electrical connection between the LIG and the copper electrode pad. We mitigated the effects of thermal oxidation and resistance from the copper electrode pad by optimizing the resistance value via alteration of the weight ratio of the CuNPs and GNP. The hybrid CuNPs/GNPs ink composition with a 98:2 ratio demonstrated superior electrical resistance and thermal oxidation characteristics compared with other mixtures. To further comprehend the chemical and physical properties of the materials, we assessed the crystal structure and phase purity pre- and postlaser irradiation, as well as IPL sintering. Notably, the porous graphene-based sensor exclusively responds to RH, not temperature variation or other interfering gases. The LIG sensor exhibited a notable sensing response of 92% at a RH level of 67%. The LIG sensor showed minimal sensing responses of 0.4, 1.87, 0.102, 0.12, and 0.29% when exposed to 200 ppm of NH_3 and $\text{CH}_3\text{CH}_2\text{OH}$, and 10, 50, and 50 ppm of CO , SO_2 , and NO_2 , respectively. The sensor responses consistently remained within a range of 91.25 ± 4.61 , demonstrating the sensor's long-term stability. Further emphasizing its reliability, the reproducibility of these LIG sensors was rigorously assessed under controlled conditions of 40% RH at 25 °C over five distinct cycles. The LOD for the LIG sensor was calculated to be 6.1% RH, indicating its exceptional sensitivity to detecting low humidity levels at room temperature. Thus, the proposed sensor platform is suitable for wearable devices to monitor human respiration patterns including slow, normal, and rapid breath rates. The sensor consistently detected human respiratory patterns for 30 min. During the tests, the observed respiratory periodicities of a volunteer breathing at slow, normal, and rapid rates were recorded as 10, 5, and 1.4 s, respectively. By distinguishing individual respiratory cycles into separate inhalation and exhalation phases, we can derive important insights into respiratory rhythm disruption during sleep. The sensor response analysis reveals that resistance increases and decreases correspond exclusively to the high humidity levels of exhaled air and low humidity levels of inhaled air, respectively. Consequently, we can infer durations of inhalation, exhalation, apnea, and various respiration rates from the alterations in sensor resistance under the respective respiratory conditions. While the porous graphene-based humidity sensor shows potential for applications in human healthcare and activity monitoring, the development of accompanying circuitry and algorithms is necessary to facilitate a comprehensive system for future commercialization.

ASSOCIATED CONTENT

Supporting Information

The Supporting Information is available free of charge at <https://pubs.acs.org/doi/10.1021/acsanm.3c05283>.

Effect of the copper and graphene nanoplatelet composition on the oxidation resistance of the

conductive pad; specific ink compositions used for the fabrication of the conductive pad; morphological and crystal structure analyses of the as-prepared conductive pad at different CuNPs/GNPs hybrid composite before and after IPL sintering; XPS analysis of PI and LIG; quantitative analysis of the baseline resistance of the fabricated LIG sensor subjected to varying degrees of flexural strain at specific bending angles; sensitivity, reliability, and reproducibility of the LIG sensor; and selectivity analysis (PDF)

AUTHOR INFORMATION

Corresponding Authors

Dong-Weon Lee – MEMS and Nanotechnology Laboratory, School of Mechanical Engineering, Chonnam National University (CNU), Gwangju 61186, Republic of Korea; Advanced Medical Device Research Center for Cardiovascular Disease and Center for Next-Generation Sensor Research and Development, Chonnam National University (CNU), Gwangju 61186, Republic of Korea; orcid.org/0000-0002-6624-6949; Email: mems@jnu.ac.kr

Changyong Yim – Department of Energy Materials & Chemical Engineering, Kyungpook National University (KNU), Sangju-si, Gyeongsangbuk-do 37224, Republic of Korea; Department of Energy Chemical Engineering and Department of Advanced Science and Technology Convergence, Kyungpook National University (KNU), Sangju-si, Gyeongsangbuk-do 37224, Republic of Korea; orcid.org/0000-0001-5987-9580; Email: cy.yim@knu.ac.kr

Authors

Changung Paeng – Department of Energy Materials & Chemical Engineering, Kyungpook National University (KNU), Sangju-si, Gyeongsangbuk-do 37224, Republic of Korea

Arun Kumar Shanmugasundaram – MEMS and Nanotechnology Laboratory, School of Mechanical Engineering, Chonnam National University (CNU), Gwangju 61186, Republic of Korea; Advanced Medical Device Research Center for Cardiovascular Disease, Chonnam National University (CNU), Gwangju 61186, Republic of Korea

Gunwoo We – Department of Energy Chemical Engineering, Kyungpook National University (KNU), Sangju-si, Gyeongsangbuk-do 37224, Republic of Korea

Taewook Kim – Department of Energy Materials & Chemical Engineering, Kyungpook National University (KNU), Sangju-si, Gyeongsangbuk-do 37224, Republic of Korea; Department of Energy Chemical Engineering and Department of Advanced Science and Technology Convergence, Kyungpook National University (KNU), Sangju-si, Gyeongsangbuk-do 37224, Republic of Korea

Jongsung Park – Department of Advanced Science and Technology Convergence and Department of Precision Mechanical Engineering, Kyungpook National University (KNU), Sangju-si, Gyeongsangbuk-do 37224, Republic of Korea

Complete contact information is available at: <https://pubs.acs.org/doi/10.1021/acsanm.3c05283>

Author Contributions

C.P. and A.S. contributed equally to this work. C. P.: Conceptualization, investigation, validation, formal analysis, data curation, and visualization. A. S.: Conceptualization, investigation, validation, formal analysis, data curation, visualization, writing—original draft, and review and editing. G. W.: Formal analysis and data curation. T. K.: Formal analysis, data curation, and visualization. J. P.: Formal analysis, data curation, and visualization. D.-W. L.: Supervision, funding acquisition, conceptualization, and writing—review and editing. C. Y.: Supervision, funding acquisition, conceptualization, and writing—review and editing.

Notes

The authors declare no competing financial interest.

ACKNOWLEDGMENTS

This work was supported by the National Research Foundation of Korea (NRF) grant funded by the Korean government (MSIT) (nos. RS-2022-00165505, 2020R1A5A8018367, and NRF-2021R1A5A8033165).

REFERENCES

- (1) Yang, Z.; Zhang, Z.; Liu, K.; Yuan, Q.; Dong, B. Controllable Assembly of SnO₂ Nanocubes onto TiO₂ Electrospun Nanofibers toward Humidity Sensing Applications. *J. Mater. Chem. C* **2015**, *3* (26), 6701–6708.
- (2) Jing, Q.; Gong, C.; Bian, W.; Tian, Q.; Zhang, Y.; Chen, N.; Xu, C.; Sun, N.; Wang, X.; Li, C.; Dou, H.; An, Y.; Liu, S.; Yu, J.; Wang, L.; Li, P.; Han, S.; Qian, D.; Liu, B. Ultrasensitive Chemiresistive Gas Sensor Can Diagnose Asthma and Monitor Its Severity by Analyzing Its Biomarker H₂S: An Experimental, Clinical, and Theoretical Study. *ACS Sens.* **2022**, *7* (8), 2243–2252.
- (3) Ayala, G. X.; Gillette, C.; Williams, D.; Davis, S.; Yeatts, K. B.; Carpenter, D. M.; Sleath, B. A Prospective Examination of Asthma Symptom Monitoring: Provider, Caregiver and Pediatric Patient Influences on Peak Flow Meter Use. *J. Asthma* **2014**, *51* (1), 84–90.
- (4) Liu, H.; Allen, J.; Zheng, D.; Chen, F. Recent Development of Respiratory Rate Measurement Technologies. *Physiol. Meas.* **2019**, *40* (7), 07TR01.
- (5) Wada, H.; Nakano, Y.; Nagao, T.; Osawa, M.; Yamada, H.; Sakaguchi, C.; Matsumoto, T.; Tsutamoto, T.; Ito, M.; Horie, M. Detection and Prevalence of Chronic Obstructive Pulmonary Disease in a Cardiovascular Clinic: Evaluation Using a Hand Held FEV₁/FEV₆ Meter and Questionnaire. *Respirology* **2010**, *15* (8), 1252–1258.
- (6) Wang, Y.; Zhang, L.; Zhang, Z.; Sun, P.; Chen, H. High-Sensitivity Wearable and Flexible Humidity Sensor Based on Graphene Oxide/Non-Woven Fabric for Respiration Monitoring. *Langmuir* **2020**, *36* (32), 9443–9448.
- (7) Tavares E Castro, A.; Matos, P.; Tavares, B.; Matos, M. J.; Segorbe-Luís, A. Alternative Functional Criteria to Assess Airflow-Limitation Reversibility in Asthma. *Rev. Port. Pneumol.* **2015**, *21* (2), 69–75.
- (8) Jin, X.; Zha, L.; Wang, F.; Wang, Y.; Zhang, X. Fully Integrated Wearable Humidity Sensor for Respiration Monitoring. *Front. Bioeng. Biotechnol.* **2022**, *10*, 1070855.
- (9) Zhang, D.; Sun, Y.; Li, P.; Zhang, Y. Facile Fabrication of MoS₂-Modified SnO₂ Hybrid Nanocomposite for Ultrasensitive Humidity Sensing. *ACS Appl. Mater. Interfaces* **2016**, *8* (22), 14142–14149.
- (10) Pascariu, P.; Airinei, A.; Oлару, N.; Petrila, I.; Nica, V.; Sacarescu, L.; Tudorache, F. Microstructure, Electrical and Humidity Sensor Properties of Electrospun NiO-SnO₂ Nanofibers. *Sens. Actuators, B* **2016**, *222*, 1024–1031.
- (11) Xiao, X.; Zhang, Q.-J.; He, J.-H.; Xu, Q.-F.; Li, H.; Li, N.-J.; Chen, D.-Y.; Lu, J.-M. Polysquaraines: Novel Humidity Sensor Materials with Ultra-High Sensitivity and Good Reversibility. *Sens. Actuators, B* **2018**, *255*, 1147–1152.
- (12) Dong, W.; Ma, Z.; Duan, Q. Preparation of Stable Crosslinked Polyelectrolyte and the Application for Humidity Sensing. *Sens. Actuators, B* **2018**, *272*, 14–20.
- (13) Li, X.; Guo, Y.; Meng, J.; Li, X.; Li, M.; Gao, D. Self-Powered Carbon Ink/Filter Paper Flexible Humidity Sensor Based on Moisture-Induced Voltage Generation. *Langmuir* **2022**, *38* (27), 8232–8240.
- (14) Duan, Z.; Jiang, Y.; Yan, M.; Wang, S.; Yuan, Z.; Zhao, Q.; Sun, P.; Xie, G.; Du, X.; Tai, H. Facile, Flexible, Cost-Saving, and Environment-Friendly Paper-Based Humidity Sensor for Multifunctional Applications. *ACS Appl. Mater. Interfaces* **2019**, *11* (24), 21840–21849.
- (15) Li, T.; Li, L.; Sun, H.; Xu, Y.; Wang, X.; Luo, H.; Liu, Z.; Zhang, T. Porous Ionic Membrane Based Flexible Humidity Sensor and Its Multifunctional Applications. *Advanced Science* **2017**, *4* (5), 1600404.
- (16) Guo, F.; Shi, W.; Wang, H.; Han, M.; Guan, W.; Huang, H.; Liu, Y.; Kang, Z. Study on highly enhanced photocatalytic tetracycline degradation of type II AgI/CuBi₂O₄ and Z-scheme AgBr/CuBi₂O₄ heterojunction photocatalysts. *J. Hazard. Mater.* **2018**, *349*, 111–118.
- (17) Wu, J.; Wu, Z.; Xu, H.; Wu, Q.; Liu, C.; Yang, B.-R.; Gui, X.; Xie, X.; Tao, K.; Shen, Y.; Miao, J.; Norford, L. K. An Intrinsically Stretchable Humidity Sensor Based on Anti-Drying, Self-Healing and Transparent Organohydrogels. *Mater. Horiz.* **2019**, *6* (3), 595–603.
- (18) Guo, H.; Lan, C.; Zhou, Z.; Sun, P.; Wei, D.; Li, C. Transparent, Flexible, and Stretchable WS₂ Based Humidity Sensors for Electronic Skin. *Nanoscale* **2017**, *9* (19), 6246–6253.
- (19) Xie, B.; You, H.; Qian, H.; Hao, S.; Li, Z.; Qin, Y.; Wen, H.-M.; Xia, S.; Xiang, Y.; Hu, J. High-Performance Flexible Humidity Sensor Based on MoO_x Nanoparticle Films for Monitoring Human Respiration and Non-Contact Sensing. *ACS Appl. Nano Mater.* **2023**, *6* (8), 7011–7021.
- (20) Hou, M.; Wang, N.; Chen, Y.; Ou, Z.; Chen, X.; Shen, F.; Jiang, H. Laser-Induced Graphene Coated Hollow-Core Fiber for Humidity Sensing. *Sens. Actuators, B* **2022**, *359*, 131530.
- (21) Ding, H.; Wei, Y.; Wu, Z.; Tao, K.; Ding, M.; Xie, X.; Wu, J. Recent Advances in Gas and Humidity Sensors Based on 3D Structured and Porous Graphene and Its Derivatives. *ACS Mater. Lett.* **2020**, *2* (11), 1381–1411.
- (22) Wang, F.; Wang, K.; Zheng, B.; Dong, X.; Mei, X.; Lv, J.; Duan, W.; Wang, W. Laser-Induced Graphene: Preparation, Functionalization and Applications. *Mater. Technol.* **2018**, *33* (5), 340–356.
- (23) C Claro, P. I.; Pinheiro, T.; Silvestre, S. L.; Marques, A. C.; Coelho, J.; Marconcini, J. M.; Fortunato, E.; C Mattoso, L. H.; Martins, R. Sustainable Carbon Sources for Green Laser-Induced Graphene: A Perspective on Fundamental Principles, Applications, and Challenges. *Appl. Phys. Rev.* **2022**, *9* (4), 041305.
- (24) Pinheiro, T.; Rosa, A.; Ornelas, C.; Coelho, J.; Fortunato, E.; Marques, A. C.; Martins, R. Influence of CO₂ Laser Beam Modelling on Electronic and Electrochemical Properties of Paper-Based Laser-Induced Graphene for Disposable pH Electrochemical Sensors. *Carbon Trends* **2023**, *11*, 100271.
- (25) Carvalho, A. F.; Fernandes, A. J. S.; Martins, R.; Fortunato, E.; Costa, F. M. Laser-Induced Graphene Piezoresistive Sensors Synthesized Directly on Cork Insoles for Gait Analysis. *Adv. Mater. Technol.* **2020**, *5* (12), 2000630.
- (26) Stanford, M. G.; Yang, K.; Chyan, Y.; Kittrell, C.; Tour, J. M. Laser-Induced Graphene for Flexible and Embeddable Gas Sensors. *ACS Nano* **2019**, *13* (3), 3474–3482.
- (27) Huang, L.; Xu, S.; Wang, Z.; Xue, K.; Su, J.; Song, Y.; Chen, S.; Zhu, C.; Tang, B. Z.; Ye, R. Self-Reporting and Photothermally Enhanced Rapid Bacterial Killing on a Laser-Induced Graphene Mask. *ACS Nano* **2020**, *14* (9), 12045–12053.
- (28) Huang, L.; Liu, Y.; Li, G.; Song, Y.; Su, J.; Cheng, L.; Guo, W.; Zhao, G.; Shen, H.; Yan, Z.; Tang, B. Z.; Ye, R. Ultrasensitive, Fast-Responsive, Directional Airflow Sensing by Bioinspired Suspended Graphene Fibers. *Nano Lett.* **2023**, *23* (2), 597–605.

- (29) Jung, D.; Kim, J.; Lee, G. S. Enhanced Humidity-Sensing Response of Metal Oxide Coated Carbon Nanotube. *Sens. Actuators, A* **2015**, *223*, 11–17.
- (30) Zhu, C.; Tao, L.-Q.; Wang, Y.; Zheng, K.; Yu, J.; L, X.; Chen, X.; Huang, Y. Graphene Oxide Humidity Sensor with Laser-Induced Graphene Porous Electrodes. *Sens. Actuators, B* **2020**, *325*, 128790.
- (31) Lan, L.; Le, X.; Dong, H.; Xie, J.; Ying, Y.; Ping, J. One-Step and Large-Scale Fabrication of Flexible and Wearable Humidity Sensor Based on Laser-Induced Graphene for Real-Time Tracking of Plant Transpiration at Bio-Interface. *Biosens. Bioelectron.* **2020**, *165*, 112360.
- (32) Duy, L. X.; Peng, Z.; Li, Y.; Zhang, J.; Ji, Y.; Tour, J. M. Laser-Induced Graphene Fibers. *Carbon* **2018**, *126*, 472–479.
- (33) Liao, J.; Zhang, X.; Sun, Z.; Chen, H.; Fu, J.; Si, H.; Ge, C.; Lin, S. Laser-Induced Graphene-Based Wearable Epidermal Ion-Selective Sensors for Noninvasive Multiplexed Sweat Analysis. *Biosensors* **2022**, *12* (6), 397.
- (34) Lin, J.; Peng, Z.; Liu, Y.; Ruiz-Zepeda, F.; Ye, R.; Samuel, E. L. G.; Yacaman, M. J.; Yakobson, B. I.; Tour, J. M. Laser-Induced Porous Graphene Films from Commercial Polymers. *Nat. Commun.* **2014**, *5* (1), 5714.
- (35) Sanderson, R. T. Interrelation of Bond Dissociation Energies and Contributing Bond Energies. *J. Am. Chem. Soc.* **1975**, *97* (6), 1367–1372.
- (36) Zhu, J.; Huang, X.; Song, W. Physical and Chemical Sensors on the Basis of Laser-Induced Graphene: Mechanisms, Applications, and Perspectives. *ACS Nano* **2021**, *15* (12), 18708–18741.
- (37) Yim, C.; Sandwell, A.; Park, S. S. Hybrid Copper-Silver Conductive Tracks for Enhanced Oxidation Resistance under Flash Light Sintering. *ACS Appl. Mater. Interfaces* **2016**, *8* (34), 22369–22373.
- (38) Bastidas, D. M.; La Iglesia, V. M.; Cano, E.; Fajardo, S.; Bastidas, J. M. Kinetic Study of Formate Compounds Developed on Copper in the Presence of Formic Acid Vapor. *J. Electrochem. Soc.* **2008**, *155* (12), C578.
- (39) Parmeggiani, M.; Zaccagnini, P.; Stassi, S.; Fontana, M.; Bianco, S.; Nicosia, C.; Pirri, C. F.; Lamberti, A. PDMS/Polyimide Composite as an Elastomeric Substrate for Multifunctional Laser-Induced Graphene Electrodes. *ACS Appl. Mater. Interfaces* **2019**, *11* (36), 33221–33230.
- (40) Ye, R.; James, D. K.; Tour, J. M. Laser-Induced Graphene: From Discovery to Translation. *Adv. Mater.* **2019**, *31* (1), 1803621.
- (41) Shanmugasundaram, A.; Kim, D.-S.; Chinh, N. D.; Park, J.; Jeong, Y.-J.; Piao, J.; Kim, D.; Lee, D. W. N-/S- Dual Doped C@ZnO: An Excellent Material for Highly Selective and Responsive NO₂ Sensing at Ambient Temperatures. *Chem. Eng. J.* **2021**, *421*, 127740.
- (42) Shanmugasundaram, A. V.; V Manorama, S.; Kim, D.-S.; Jeong, Y.-J.; Weon Lee, D. Toward Point-of-Care Chronic Disease Management: Biomarker Detection in Exhaled Breath Using an E-Nose Sensor Based on rGO/SnO₂ Superstructures. *Chem. Eng. J.* **2022**, *448*, 137736.
- (43) Shanmugasundaram, A.; Boppella, R.; Jeong, Y.-J.; Park, J.; Kim, Y.-B.; Choi, B.; Park, S. H.; Jung, S.; Lee, D.-W. Facile In-Situ Formation of rGO/ZnO Nanocomposite: Photocatalytic Remediation of Organic Pollutants under Solar Illumination. *Mater. Chem. Phys.* **2018**, *218*, 218–228.
- (44) Shanmugasundaram, A.; Chinh, N. D.; Jeong, Y.-J.; Hou, T. F.; Kim, D.-S.; Kim, D.; Kim, Y.-B.; Lee, D.-W. Hierarchical Nanohybrids of B- and N-Codoped Graphene/Mesoporous NiO Nanodisks: An Exciting New Material for Selective Sensing of H₂S at near Ambient Temperature. *J. Mater. Chem. A* **2019**, *7* (15), 9263–9278.
- (45) Vivaldi, F. M.; Dallinger, A.; Bonini, A.; Poma, N.; Sembranti, L.; Biagini, D.; Salvo, P.; Greco, F.; Di Francesco, F. Three-Dimensional (3D) Laser-Induced Graphene: Structure, Properties, and Application to Chemical Sensing. *ACS Appl. Mater. Interfaces* **2021**, *13* (26), 30245–30260.
- (46) Mushtaq, N.; Chen, G.; Sidra, L. R.; Fang, X. Organosoluble and High T_g Polyimides from Asymmetric Diamines Containing N-Amino and N-Aminophenyl Naphthalimide Moieties. *RSC Adv.* **2016**, *6* (30), 25302–25310.
- (47) Abdulhafez, M.; Tomaraei, G. N.; Bedewy, M. Fluence-Dependent Morphological Transitions in Laser-Induced Graphene Electrodes on Polyimide Substrates for Flexible Devices. *ACS Appl. Nano Mater.* **2021**, *4* (3), 2973–2986.
- (48) Getachew, B. A.; Bergsman, D. S.; Grossman, J. C. Laser-Induced Graphene from Polyimide and Polyethersulfone Precursors as a Sensing Electrode in Anodic Stripping Voltammetry. *ACS Appl. Mater. Interfaces* **2020**, *12* (43), 48511–48517.
- (49) Huang, L.; Cheng, L.; Ma, T.; Zhang, J.; Wu, H.; Su, J.; Song, Y.; Zhu, H.; Liu, Q.; Zhu, M.; Zeng, Z.; He, Q.; Tse, M.; Yang, D.; Yakobson, B. I.; Tang, B. Z.; Ren, Y.; Ye, R. Direct Synthesis of Ammonia from Nitrate on Amorphous Graphene with Near 100% Efficiency. *Adv. Mater.* **2023**, *35* (24), 2211856.
- (50) Liu, Y. J.; Hao, L. Z.; Gao, W.; Liu, Y. M.; Li, G. X.; Xue, Q. Z.; Guo, W. Y.; Yu, L. Q.; Wu, Z. P.; Liu, X. H.; Zeng, H. Z.; et al. Growth and Humidity-Dependent Electrical Properties of Bulk-like MoS₂ Thin Films on Si. *RSC Adv.* **2015**, *5*, 74329–74335.
- (51) Pang, Y.; Jian, J.; Tu, T.; Yang, Z.; Ling, J.; Li, Y.; Wang, X.; Qiao, Y.; Tian, H.; Yang, Y.; Ren, T.-L. Wearable Humidity Sensor Based on Porous Graphene Network for Respiration Monitoring. *Biosens. Bioelectron.* **2018**, *116*, 123–129.
- (52) Zhang, D.; Tong, J.; Xia, B. Humidity-Sensing Properties of Chemically Reduced Graphene Oxide/Polymer Nanocomposite Film Sensor Based on Layer-by-Layer Nano Self-Assembly. *Sens. Actuators, B* **2014**, *197*, 66–72.
- (53) Huang, Q.; Zeng, D.; Tian, S.; Xie, C. Synthesis of Defect Graphene and Its Application for Room Temperature Humidity Sensing. *Mater. Lett.* **2012**, *83*, 76–79.
- (54) Phan, D.-T.; Park, I.; Park, A.-R.; Park, C.-M.; Jeon, K.-J. Black P/Graphene Hybrid: A Fast Response Humidity Sensor with Good Reversibility and Stability. *Sci. Rep.* **2017**, *7* (1), 10561.
- (55) Lu, Y.; Xu, K.; Yang, M.-Q.; Tang, S.-Y.; Yang, T.-Y.; Fujita, Y.; Honda, S.; Arie, T.; Akita, S.; Chueh, Y.-L.; Takei, K. Highly Stable Pd/HfNb₃O₈-Based Flexible Humidity Sensor for Perdurable Wireless Wearable Applications. *Nanoscale Horiz.* **2021**, *6* (3), 260–270.
- (56) Pawar, M. S.; Bankar, P. K.; More, M. A.; Late, D. J. Ultra-Thin V₂O₅ Nanosheet Based Humidity Sensor, Photodetector and Its Enhanced Field Emission Properties. *RSC Adv.* **2015**, *5* (108), 88796–88804.
- (57) Kondee, S.; Arayawut, O.; Pon-On, W.; Wongchoosuk, C. Nitrogen-Doped Carbon Oxide Quantum Dots for Flexible Humidity Sensor: Experimental and SCC-DFTB Study. *Vacuum* **2022**, *195*, 110648.
- (58) Zhao, Q.; Yuan, Z.; Duan, Z.; Jiang, Y.; Li, X.; Li, Z.; Tai, H. An Ingenious Strategy for Improving Humidity Sensing Properties of Multi-Walled Carbon Nanotubes via Poly-L-Lysine Modification. *Sens. Actuators, B* **2019**, *289*, 182–185.
- (59) Gupta, S. P.; Pawbake, A. S.; Sathe, B. R.; Late, D. J.; Walke, P. S. Superior Humidity Sensor and Photodetector of Mesoporous ZnO Nanosheets at Room Temperature. *Sens. Actuators, B* **2019**, *293*, 83–92.
- (60) Lee, J.-U.; Ma, Y.-W.; Jeong, S.-Y.; Shin, B.-S. Direct Fabrication of Ultra-Sensitive Humidity Sensor Based on Hair-Like Laser-Induced Graphene Patterns. *Micromachines* **2020**, *11* (5), 476.
- (61) Choi, J.; Baek, S.; Jeon, S.; Yim, C. Laser-Induced Graphene on a Quartz Crystal Microbalance for Humidity Sensing. *Crystals* **2021**, *11* (3), 289.